The Astrophysical Journal, 611:434–451, 2004 August 10

A STEADY, RADIATIVE-SHOCK METHOD FOR COMPUTING X-RAY EMISSION FROM COLLIDING STELLAR WINDS IN CLOSE, MASSIVE-STAR BINARIES

I. I. Antokhin[1]
Department of Physics and Astronomy, Kelvin Building, University of Glasgow, Glasgow G12 8QQ, UK; igor@astro.gla.ac.uk

S. P. Owocki[2]
Bartol Research Institute, University of Delaware, Newark, DE 19716; owocki@bartol.udel.edu

AND

J. C. Brown
Department of Physics and Astronomy, Kelvin Building, University of Glasgow, Glasgow G12 8QQ, UK; john@astro.gla.ac.uk
Received 2004 February 3; accepted 2004 April 21

ABSTRACT

We present a practical, efficient, semianalytic formalism for computing steady state X-ray emission from radiative shocks between colliding stellar winds in relatively close (orbital period up to order tens of days) massive-star, binary systems. Our simplified approach idealizes the individual wind flows as smooth and steady, ignoring the intrinsic instabilities and associated structure thought to occur in such flows. By also suppressing thin-shell instabilities for wind-collision radiative shocks, our steady state approach avoids the extensive structure and mixing that has thus far precluded reliable computation of X-ray emission spectra from time-dependent hydrodynamical simulations of close-binary, wind-collision systems; but in ignoring the unknown physical level of such mixing, the luminosity and hardness of X-ray spectra derived here represent upper limits to what is possible for a given set of wind and binary parameters. A key feature of our approach is the separation of calculations for the small-scale shock-emission from the ram-pressure–balance model for determining the large-scale, geometric form of the wind-wind interaction front. Integrating the localized shock emission over the full interaction surface and using a warm-absorber opacity to take account of attenuation by both the smooth wind and the compressed, cooled material in the interaction front, the method can predict spectra for a distant observer at any arbitrary orbital inclination and phase. We illustrate results for a sample selection of wind, stellar, and binary parameters, providing both full X-ray light curves and detailed spectra at selected orbital phases. The derived spectra typically have a broad characteristic form, and by synthetic processing with the standard XSPEC package, we demonstrate that they simply cannot be satisfactorily fitted with the usual attenuated single- or two-temperature thermal-emission models. We conclude with a summary of the advantages and limitations of our approach and outline its potential application for interpreting detailed X-ray observations from close, massive-star binary systems.

Subject headings: binaries: general — stars: winds, outflows — stars: early-type — stars: mass loss — stars: X-rays

Online material: color figures

1. INTRODUCTION

Massive, hot, luminous stars—those of type OB and WR—have strong, high-speed, radiatively driven stellar winds. In the many binary systems consisting of two massive stars, collision of the individual stellar winds leads to formation of strong shock fronts, in which the kinetic energy of the high-speed (>1000 km s^{-1}) wind flows is converted into high-temperature (>10 MK) gas capable of emitting moderately hard X-rays (>1 keV). Efforts to develop dynamical simulations of colliding-wind X-ray emission have been quite successful for the *adiabatic* shocks characteristic of the relatively low densities at interaction fronts of *wide*-binary systems (Stevens et al. 1992; Zhekov & Skinner 2000; Pittard et al. 2002), but such numerical simulations encounter severe difficulties in resolving the extensive structure of unstable *radiative* shocks (e.g., Langer et al. 1981; Chevalier & Imamura 1982; Myasnikov et. al. 1998; Walder & Folini 2000) that occur at the higher interaction-densities of *close* binaries (Stevens et al. 1992; Pittard & Stevens 1997; Pittard 1998).

A principal goal of this paper is to address this latter shortcoming. By applying detailed planar shock emission calculations within simplified, steady state models for the wind-interaction front geometry, we derive X-ray emission spectra for close-binary systems with a range of wind and stellar parameters.

In hydrodynamical simulations of colliding winds in close binaries, the inherent instability of the resulting radiative shocks leads to extensive variability and structure, inducing substantial mixing between hot and cool material. The associated reduction in hot material can significantly reduce the hardness of the associated radiative emission, even shifting it from the X-ray into the XUV or EUV spectral domains. Unfortunately, the physically appropriate degree of mixing is difficult to predict a priori. Because of numerical diffusion and the inherently limited resolution of the spatial grid, the level of mixing in simulation models may likely overestimate what

[1] Current address: Sternberg Astronomical Institute, Moscow University, Universitetskij Prospect 13, Moscow 119899, Russia.
[2] PPARC Visiting Fellow, Department of Physics and Astronomy, University of Glasgow, Glasgow G12 8QQ, UK.

occurs in actual colliding wind systems. Moreover, magnetic fields and/or plasma effects not accounted for in such idealized hydrodynamical simulations could stabilize the interaction region and so reduce the mixing. Indeed, the sometimes quite hard X-ray emission observed from some close binary systems indicates that the level of mixing must in these cases be quite limited. A good indicator of the hard thermal X-ray emission is the presence in an X-ray spectrum of the 6.4–6.7 keV Fe emission-line complex. This complex is observed, e.g., in the binaries WR 139 (Maeda et al. 1999), η Car (Pittard & Corcoran 2002), ι Ori (Pittard et al. 2000), and so on (for the full list and discussion, see Raassen et al. 2003).

Given this uncertainty regarding the importance of mixing and the computational expense of running numerical simulation models, analyses of observed X-ray spectra from colliding wind systems have often defaulted to applying generic plasma emission codes (e.g., XSPEC; Arnaud 1996[3]) assuming one or more discrete temperatures.

This paper aims to provide an intermediate alternative that accounts for the detailed form of the wind collision shock, but within a relatively simple, smooth, steady state model that *ignores* any mixing. Under the further idealization that the wind density is high enough to make the shock purely radiative, the model also ignores losses associated with adiabatic expansion of the postshock gas. By thus assuming that the entire energy dissipated in the shock is radiated away at temperatures ranging up to the immediate postshock value, the derived spectra should represent an *upper limit* to the level and hardness of radiation within the bandpass of orbiting X-ray telescopes such as *Chandra* and *XMM*.

Because of this assumption of thin, radiative shocks, our approach only applies to dense winds in relatively close binary systems, with periods ranging up to tens of days. In § 3.4 we give explicit expressions (see eqs. [23] and [24]) for the applicable binary separation and period and how these scale with wind speed and mass-loss rate (see also eq. [8] of Stevens et al. 1992).

In addition to this suppression of unresolvable structure and mixing, a key advantage to our approach stems from its *separation* of the small-scale shock-emission calculation from the model for the large-scale, geometric form of the wind-wind interaction front. In our idealization of laminar, steady, radiative shocks, the postshock, radiative-cooling layer is presumed to be geometrically thin compared to any competing scale, for example the binary separation, or the radius of curvature for the interaction front. Moreover, the timescale for shock-heated material to cool is likewise presumed to be small compared with the time required for the flow to advect along a substantial arc of the curved front. This justifies neglect of the adiabatic cooling from wind expansion, which would effectively couple the internal evolution of the shock to global wind structure. It also implies that nearly all[4] of the incoming kinetic energy from the wind flow normal to the front is locally converted into radiative emission in the postshock region. This allows an "on-the-spot" treatment of the radiative emission at each location along the front.

This local emission is derived from a simple, steady, *planar*-shock model that, given the velocity and kinetic energy flux associated with flow normal to the local interaction front, yields both the spectrum and overall level of radiation emitted over the full shock-cooling layer. In this approach, the *contact surface*, which separates the distinct material from each wind and which lies within the interaction front, acts effectively as fixed barrier or wall that stops the normal component of the incoming wind flow. In the idealization that the interaction region between the initial wind shock and this contact-surface wall is geometrically thin, this incoming wind can moreover be treated as locally planar, i.e., neglecting the global divergence associated with the spherical wind expansion. Since in this thin-cooling-layer picture the overall interaction front is closely aligned with the contact surface, our descriptions below of their overall form treat them as effectively synonymous.

In the hot region immediately behind the initial adiabatic shock, the velocity (density) is decreased (increased) by a maximum factor of 4 (for the assumed case of a monatomic gas with ratio of specific heats $\gamma = 5/3$), but then within a nearly isobaric cooling layer, the gas is gradually slowed to an effective stop as cooled, dense material piles up against the fixed wall (see § 3). We apply an extensive atomic database to compute the spectral emission and associated cooling, and integrate this throughout the layer from the shock to the wall. The resulting code for computing the cumulative shock emission spectrum constitutes one key component for the study here.

In this initial work, the spectra we derive are moderate-resolution and do not account for the detailed form of the emission profile from individual lines. In principle, such profiles could be derived for modeling very high resolution spectra, following the general approach used by Henley et al. (2003). However, note that none of the binary systems observed with *Chandra* or *XMM* appear to have high enough X-ray brightness to give sufficient signal to resolve individual line profiles.

A second key component of our approach regards the model for the interaction front. As detailed in § 2, the overall geometric form of this front is derived from integration of a first-order, ordinary differential equation that accounts for the ram-pressure balance associated with the relative momentum flux of the two winds. This approach builds on previous analyses (see, e.g. Huang & Weigert 1982; Giuliani 1982; Girard & Willson 1987; Usov 1992; Canto et al. 1996) but uses simple "beta" velocity-laws to take account of the possibility that, in such close-binary systems, the wind speeds may have not yet reached their terminal values at the interaction front. Such a simple beta velocity-law provides a quite accurate representation of the velocity variation in full dynamical wind models (see, e.g., Pauldrach et al. 1986), with index β typically of order unity, while still allowing the flexibility to examine cases in which the acceleration to terminal speed occurs near the star (lower β) or over a more extended region (higher β).

In practice, we first apply our planar shock emission code to tabulate the detailed emitted energy spectrum as a function of just a single parameter representing the shock strength, namely, the postshock temperature (which depends on the square of the normal component of incoming flow velocity; § 3). The overall level of emission is then adjusted according to the local density, so that the total, spectrally integrated flux equals the dissipated kinetic energy flux density normal to the front. Using the simple wind-momentum–balance model for the overall interaction front (§ 2), the local emission from both wind shocks at each differential patch is then accumulated to provide

[3] See http://asds.stsci.edu/packages/analysis/XANADU.html.

[4] A small fraction, ca. 1/16, goes into mechanical work in compressing the dense, cooled layer, but we generally ignore this in our simplified treatment below; see § 3.

a global model for the wind-wind X-ray emission (§ 4). To provide a basis for modeling the attenuation of emitted X-rays by cooler material, we analyze the column densities of cooled material in the interface (§ 4.3 and Appendix) and develop a simple, fixed, warm-absorber model (§ 4.4) for the opacity. After developing a context for the intrinsic properties and characteristics of the basic wind-collision models (§ 5), we combine all aspects to derive predictions for the observed X-ray spectrum as a function of phase and inclination angle (§ 6).

In § 7 we convolve a sample synthetic spectrum with the *XMM-Newton* response functions, to analyze it in the standard observer's X-ray package XSPEC, and then compare the inferred physical parameters with their actual values in the assumed models. Finally, § 8 summarizes the strengths and weaknesses of our approach, with an eye toward its further development and application in future work.

2. INTERACTION FRONT

The shape of the interaction front in a colliding wind binary in a steady state approach has been extensively discussed in the literature, using both analytic analyses (see, e.g. Huang & Weigert 1982; Giuliani 1982; Girard & Willson 1987; Usov 1992; Canto et al. 1996) and numerical simulations (e.g., Luo et al. 1990; Myasnikov & Zhekov 1993; Stevens et al. 1992; Walder 1995; Pittard & Stevens 1997; Walder & Folini 2003). Generally, the overall form of the interaction front is in good agreement between these numerical and analytic analyses (Pittard & Stevens 2002).

One complicating factor regards the role of orbital motion, which makes the overall structure inherently three-dimensional and thus much more difficult to model or simulate. On scales larger than the binary separation, such orbital motion wraps the wind interaction front into a spiral form and as such is an essential effect. But in the region between the stars of most relevance for X-ray emission, the deflection of the interaction front is relatively small, because orbital velocities are typically no larger than a few hundred km s^{-1}, much smaller than the stellar wind speeds, which are typically a few thousand km s^{-1}. In our models we thus neglect orbital motion and associated inertial forces, so that the interaction front retains a symmetry about the axis connecting the stars and so can be described in terms of much simpler, two-dimensional model. We expect that this neglect of front deflection should have only modest effects on the resulting X-ray spectrum and luminosity, but further examination of this is left to future work.

Under the further assumption that the cooling regions of the wind interaction shocks are relatively narrow, the overall form of the *interaction front* corresponds closely to that of the embedded *contact surface* separating the material from the two winds. We calculate this axisymmetric shape of the contact surface from the momentum balance of the two winds,

$$\rho_1 v_{1\perp}^2 = \rho_2 v_{2\perp}^2, \tag{1}$$

where ρ and v are the local density and wind speed. The "$\perp$" denotes components normal to the interaction surface, and, referring to Figure 1, the numerical subscripts represent evaluation at the locations $\boldsymbol{r}_1$, $\boldsymbol{r}_2$. Using mass continuity in terms of the constant wind mass-loss rates $\dot{M} \equiv 4\pi\rho v r^2$, equation (1) becomes

$$\frac{\dot{M}_1}{4\pi r_1^2} v_1 \sin^2\theta_1 = \frac{\dot{M}_2}{4\pi r_2^2} v_2 \sin^2\theta_2, \tag{2}$$

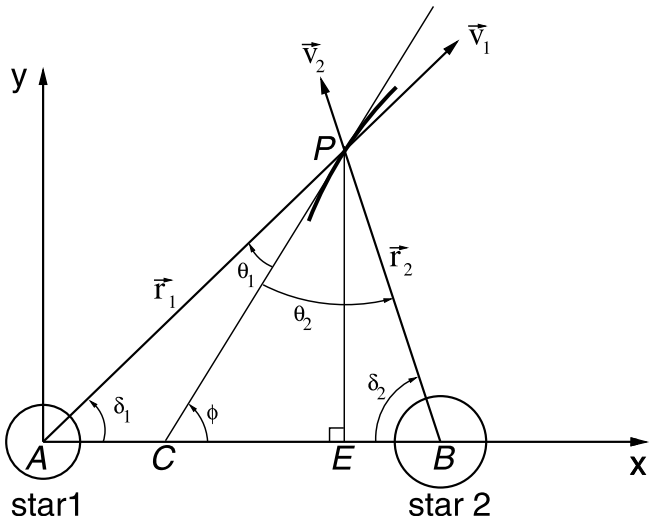

FIG. 1.—Illustration of the coordinate system used in the formulation of the wind-wind collision model. The line *CP* is tangent to the interaction front shown by the heavy line.

or with some rearrangement,

$$\frac{r_2^2 \sin^2\theta_1}{r_1^2 \sin^2\theta_2} = \frac{\dot{M}_2 v_2}{\dot{M}_1 v_1} \equiv \eta. \tag{3}$$

From ΔCPE we have the geometrical relation

$$\cot\phi = \frac{CE}{PE} = \frac{CB - (D - x)}{y}, \tag{4}$$

where D is the binary separation (*AB* in Fig. 1). This can be rewritten as

$$\frac{dx}{dy} = \frac{CB - (D - x)}{y}, \tag{5}$$

where $x(y)$ is the function describing the shape of the interaction front. To find *CB*, we can use further geometrical relations:

$$\frac{CB}{\sin\theta_2} = \frac{r_2}{\sin\phi}, \qquad \frac{(D - CB)}{\sin\theta_1} = \frac{r_1}{\sin\phi}.$$

Combining these with equation (3), we get

$$CB = \frac{D r_2^2}{r_1^2\sqrt{\eta} + r_2^2},$$

and substituting *CB* into equation (5),

$$\frac{dx}{dy} = \frac{1}{y}\left[x - \frac{D r_1^2(x,y)\sqrt{\eta(x,y)}}{r_1^2(x,y)\sqrt{\eta(x,y)} + r_2^2(x,y)}\right]. \tag{6}$$

This is an ordinary differential equation for the interaction front. The boundary condition ($dx/dy\,|_{y\to 0} \to 0$) is

$$x_0 \equiv x(0) = \frac{D}{1 + \sqrt{\eta}}.$$

In the case of constant wind velocities, equation (6) can be solved analytically, but in a close binary system the velocities v_1 and v_2 at the contact surface may not yet have reached their

terminal values, and in this case solution of equation (6) generally requires numerical integration. Moreover, in this case the momentum ratio η varies along the contact surface, and even the base position $x(0)$ must be solved by numerical root-finding.

Once equation (6) is solved, θ_1 and θ_2 and then the normal and tangential components of the velocities at any given position at the contact surface can be found. For both winds we assume velocity laws parameterized by an exponent β,

$$v_{1,2}(r) = v_{1,2\infty}\left(1 - \frac{r_{*1,2}}{r}\right)^{\beta_{1,2}}. \quad (7)$$

3. STRUCTURE AND EMISSION IN A PLANAR, POSTSHOCK COOLING LAYER

3.1. *Equations for a Nearly Isobaric Cooling Layer*

Let us now describe our approach for calculating the emission of a postshock cooling layer. As noted in the introduction, the cooling layer near the wind interaction front is modeled in terms of a planar flow against a fixed barrier or wall, as illustrated in Figure 2.

We begin by writing the general vector equation for conservation of internal energy e in a flow with vector velocity $\boldsymbol{v}$, gas pressure P, and a net volumetric energy loss Λ,

$$\frac{\partial e}{\partial t} + \nabla\cdot(e\boldsymbol{v}) + P\nabla\cdot\boldsymbol{v} = -\Lambda, \quad (8)$$

where for our assumption of an ideal monatomic gas with ratio of specific heats $\gamma = 5/3$, the energy and pressure are related by $e = P/(\gamma - 1) = 3P/2$. In terms of the combined number density $n = n_e + n_{\rm ion}$ of electrons and ions, the pressure is given by the usual ideal gas law, $P = nkT$, where T is the temperature and k is Boltzman's constant. For our case of steady, planar flow with constant number flux nv along a length l, equation (8) can thus be written as

$$\frac{5}{2}kn\boldsymbol{v}\frac{dT}{dl} - \boldsymbol{v}\frac{dP}{dl} = -\Lambda. \quad (9)$$

In the subsonic flow of a postshock cooling layer, the pressure gradient decelerates the gas from the postshock speed, as set through the momentum conservation equation

$$v\frac{dv}{dl} = -\frac{1}{\rho}\frac{dP}{dl}, \quad (10)$$

where the mass density $\rho = \mu m_p n$; μ is the mean atomic weight of the electron plus ion mixture, and m_p is the proton mass. Applying this in equation (9), we find

$$nv\frac{d}{dl}\left(\frac{5}{2}kT + \frac{\mu m_p v^2}{2}\right) = -\Lambda. \quad (11)$$

The sum in the square brackets is clearly the total energy per particle, with the first and second terms representing respectively the enthalpy and the kinetic energy. Evaluating the term in parentheses across the shock gives

$$\left(\frac{5}{2}kT_0 + \frac{\mu m_p v_0^2}{2}\right) = \frac{\mu m_p v_{0w}^2}{2}, \quad (12)$$

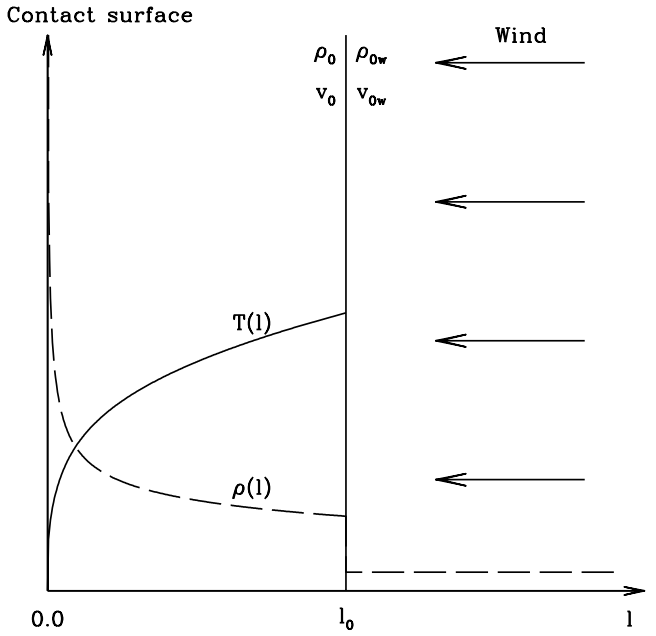

FIG. 2.—Notation and structure in a steady, planar cooling layer behind a shock that results from flow into a fixed barrier or wall. [*See the electronic edition of the Journal for a color version of this figure.*]

where the "0w" and "0" subscripts represent conditions in the immediate preshock wind and postshock flow, and we have assumed a highly supersonic wind in ignoring its internal enthalpy.

For a strong, steady, standing shock, the postshock gas pressure must balance the incoming flow "ram pressure":

$$\frac{k}{\mu m_p}\rho_0 T_0 = \rho_{0w} v_{0w}(v_{0w} - v_0). \quad (13)$$

For the strong-shock case with compression ratio $\rho_0/\rho_{0w} = v_{0w}/v_0 = 4$, this implies

$$kT_0 = \frac{3}{16}\mu m_p v_{0w}^2 = 3\mu m_p v_0^2. \quad (14)$$

Comparison with the square brackets of equations (11) and (12) shows that the former, internal-enthalpy term is a factor of 15 larger than the latter, kinetic-energy term. Tracing the latter term back to the pressure-gradient term in equation (9), we see that ignoring this pressure gradient only introduces an error of 1/16, or 6%, in the overall energy balance. As this greatly simplifies the analysis, we henceforth assume this *isobaric* approximation for the cooling layer.

3.2. *Solving for the Structure of a Radiative Cooling Layer*

Let us thus consider the isobaric form of equation (9):

$$\frac{5k}{2\mu m_p}\rho v\frac{dT}{dl} = -n_e n_{\rm H}\lambda(T). \quad (15)$$

Here we have also assumed that the energy loss Λ is solely from radiative cooling that scales as $n_e n_{\rm H}\lambda(T)$, where $\lambda(T)$ is the cooling function (Fig. 3), with its standard calibration in terms of the hydrogen number density $n_{\rm H}$. Taking advantage

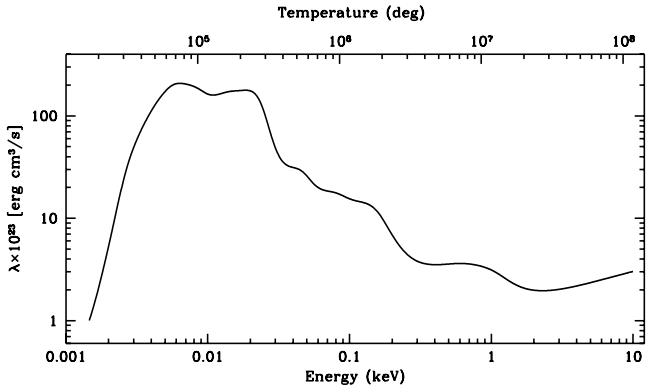

FIG. 3.—Cooling function for the standard case of solar abundances.

of the constancy of both the mass flux $\rho v = \rho_0 v_0$ and pressure P, equation (15) takes the form

$$\frac{dT}{dl} = -C(T)\frac{\lambda(T)}{T^2}. \tag{16}$$

Defining X_Z as the number fraction (to $n_{\rm ion}$) of an ion with charge Z, $X_{\rm H}$ as the corresponding number fraction for hydrogen, and $\overline{\mu}$ as the mean atomic weight of the nuclei, we find

$$C(T) = \frac{2\sum X_Z Z X_{\rm H}\mu^3 m_p P^2}{5\overline{\mu}^2 k^3 \rho_0 > v_0} = \frac{9\sum X_Z Z X_{\rm H}\mu^3 m_p}{40\overline{\mu}^2 k^3}\rho_{0w} v_{0w}^3, \tag{17}$$

where the latter equality makes use of the ram-pressure balance (eq. [13]) and assumes the strong-shock compression factor $\rho_0/\rho_{0w} = 4$. Note that C depends on temperature only through ionization changes, which alter X_Z, $\overline{\mu}$, and μ.

The cooling function $\lambda(T)$ has been computed by several authors (see, e.g., Raymond et al. 1976). However, we do not use any such precomputed functions in this study. Instead, for self-consistency, we apply the same plasma emission code used to derive the detailed X-ray spectra and simply compute the energy integral of the full radiative spectra to tabulate this total cooling function. This basic plasma emission is modeled with an optically thin thermal plasma code (Mewe et al. 1985, 1986, 1995) commonly known as the MEKAL code; this code is also used in the XSPEC program[5]—one of the most common tools used in analyzing X-ray emission spectra. In addition to temperature and density, the total radiative cooling also depends on chemical abundances, which can differ between the two winds, e.g., in a WR+O system. Figure 3 shows the cooling function computed for solar abundances. We have also computed curves with WR-like abundances. The resulting spectra and their variations with orbital phase are qualitatively similar to those computed using solar abundances. As such we choose not to present these in detail here, but note that the ability to use nonsolar abundances is available when the method is applied to specific systems for which nonsolar values are inferred.

Once this cooling function is tabulated, the temperature variation within the cooling layer can be obtained by straightforward numerical integration of equation (16), starting

[5] See http://heasarc.gsfc.nasa.gov/docs/xanadu/xspec.

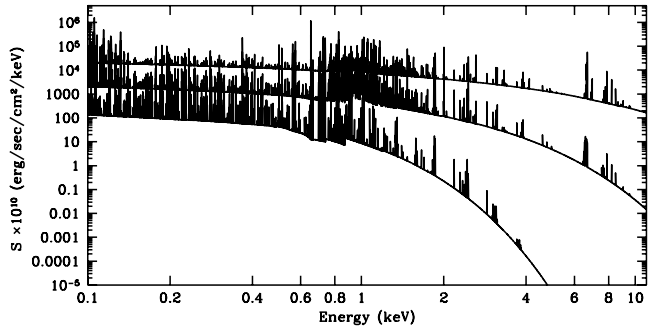

FIG. 4.—X-ray spectra from emission integrated over the full cooling zones for radiative shocks with various incoming flow speeds, namely, 500, 1000, and 2000 km s^{-1} for, respectively, the bottom, middle, and top curves. The material has solar abundances, and the emission units are for a fiducial, CGS-value of unity for the pre-shock density, i.e., $\rho = 1$ g cm^{-3}. [*See the electronic edition of the Journal for a color version of this figure.*]

with the immediate postshock temperature T_0 and extending to the assumed arbitrarily low temperature $T \to 0$ near the barrier or wall. From equation (14), the initial postshock temperature can be seen to scale as

$$kT_0 = \frac{3}{16}\mu m_p v_{0w}^2 = 1.21\left(\frac{\mu}{0.62}\right)\left(\frac{v_{0w}}{1000\ {\rm km\ s^{-1}}}\right)^2\ {\rm keV}, \tag{18}$$

where in the last equality $\mu = 0.62$ is the value appropriate for a fully ionized medium with solar abundances (Anders & Grevesse 1989).

Figure 4 shows the integrated spectra from shock cooling zones with selected values for the incoming, normal flow speed.

3.3. *Narrowness of Cooling Layer*

Both this initial postshock temperature T_0 and the function $C(T)$ (see eq. [17]) depend on the local properties of the wind impingent on the shock layer. As an initial approximation, let us ignore the thickness of the cooling layer itself and simply assume these preshock flow properties to be those of the global wind evaluated at the local interaction front. The validity of this assumption can be examined by evaluating the characteristic cooling length in the immediate postshock region,

$$l_0 \equiv \frac{T_0}{|dT/dl|_0} = \frac{T_0^3}{C\lambda(T_0)} = \frac{15\overline{\mu}^2 m_p^2}{512\sum X_Z Z X_{\rm H}}\frac{v_{0w}^3}{\rho_{0w}\lambda(T_0)}. \tag{19}$$

For the standard case of a fully ionized medium with solar abundances (Anders & Grevesse 1989), we have $\overline{\mu} = 1.3$ and $\sum X_Z Z X_{\rm H} = 0.99$. Then for an interaction front that makes a tangent angle θ with the local wind direction at a radius r from the center of its source star, we find

$$\frac{l_0}{r} \simeq 0.0194\frac{V_{1000}^4 \sin^3\theta r/R_\odot}{\dot{M}_{-6}\lambda_{-23}(T_0)} \simeq 0.01\frac{V_{1000}^5 \sin^3\theta r/R_\odot}{\dot{M}_{-6}}, \tag{20}$$

where $R_\odot$ is the solar radius, $\dot{M}_{-6}$ is the wind mass-loss rate in $10^{-6}\ M_\odot$ yr^{-1}, V_{1000} is the local wind speed in 1000 km s^{-1}, and λ_{-23} is the cooling function in 10^{-23} ergs cm^3 s^{-1}. The latter equality in equation (20) makes use of equation (18) (taking $\mu = 0.62$) and approximates the cooling function (see Fig. 3) as

$$\lambda_{-23}(T_0) \simeq 2(kT_0/{\rm keV})^{-1/2} \simeq 1.85/V_{1000}. \tag{21}$$

The categorization of whether a colliding-wind shock is *adiabatic* or *radiative* is essentially determined by whether this ratio l_0/r is substantially greater than or less than unity (see next section). This ratio is, in fact, closely related to the parameter χ (ratio of escape time to cooling time) defined by Stevens et al. (1992; see their eq. [8]), with the same scaling and similar numerical value.

For many contexts, it is useful to identify an associated column mass $\sigma_{\rm hot} \equiv l_0 \rho_{0w}$ required for this hot layer to cool,

$$\sigma_{\rm hot} = 0.0141 \ \frac{V_{1000}^3 \sin^3\theta}{\lambda_{-23}(T_0)} \simeq 0.0077 V_{1000}^4 \sin^4\theta \frac{\rm cm^2}{\rm g}, \quad (22)$$

where the latter equality again makes use of equation (21).

Actually, because of the steep temperature dependence of isobaric cooling, the integrated cooling length from the shock to the fixed wall is somewhat *smaller* than l_0. For example, if we approximate the cooling function by the high-temperature scaling $\lambda(T) \sim T^{-1/2}$ (see Fig. 3), integration over the isobaric layer shows that the total cooling length from shock to wall is $2l_0/7$.

In our full numerical code, we use a simple iterative procedure to take self-consistent account of the finite cooling layer thickness in determining the input density and velocity of the wind impingent on the shock. Even for the massive, close binaries considered in this paper, the ratio of cooling length to radius is not always very small (see Fig. 10), but it is generally below unity, and this appears sufficient to ensure convergence within a few iterations.

3.4. *Orbital Period Limit for Applicability of Radiative Shock Method*

The above analysis of cooling length widths allows us to identify the typical orbital periods for which this thin, radiative shock formalism can potentially be applicable. Specifically, let us identify a characteristic radius r with the orbital semimajor axis, i.e., $r \approx a$. Then, to ensure that the above iteration procedure convergences, let us require that $l_0 < r$, yielding from equation (20)

$$a < 100 R_\odot \frac{\dot{M}_{-6}}{V_{1000}^5}, \quad (23)$$

where we have taken the case of normal incidence ($\sin\theta = 1$). Using Kepler's third law, this can alternatively be written in terms of a constraint on the observed period,

$$P < 26 \ {\rm day} \left(\frac{20 \ M_\odot}{M_1 + M_2} \right)^{1/2} \frac{\dot{M}_{-6}^{1.5}}{V_{1000}^{7.5}}. \quad (24)$$

This thus gives an explicit estimate of the orbital period domain of applicability of our method, but note in particular the very strong dependence on the preshock velocity. For example, just a 10% higher preshock wind speed (i.e., 1100 km s^{-1}) reduces the maximum applicable period by a factor of 2!

Constraint (24) represents the requirement for applicability of the method over the full orbit; for systems with somewhat longer orbital periods but significant eccentricity, there can also be limited applicability near periastron.

4. COMPUTING THE CUMULATIVE EMISSION FROM THE INTERACTION ZONE

4.1. *Optically Thin Case*

Once the shape of the interaction front and the width of the two cooling layers are computed, one can calculate the normal components of the wind velocities and the wind densities at any given point of the front. Then the X-ray emission of each areal segment of the front can be calculated via look up in a precomputed table of spectra of planar cooling layers, interpolating the temperature-tabulated spectra according to the local normal component of the wind velocity and scaling the brightness according to the local wind density, which sets the associated kinetic energy flux density input from the wind.

Assuming the energy is emitted isotropically from this cooling layer, and noting from the axial symmetry that this local emission should only depend on the axial coordinate y (see Fig. 1), let us define $S(y, E)$ to be the local spectral emission at energy E per unit area of front surface. Integration over each ring of area $2\pi y\, dy/\sin\phi$ then yields the total luminosity spectrum emitted by the interaction front:

$$L(E) = 2\pi \int_0^\infty \frac{S(y, E)}{\sin\phi} y\, dy. \quad (25)$$

Ignoring absorption, the flux spectrum detected by an observer at a large distance R ($\gg D$, the binary separation) is then just $F(E) = L(E)/4\pi R^2$.

4.2. *Accounting for Absorption by Cool/Warm Material*

More generally, it can be important to take account of absorption of the X-rays, particularly by cooler (or "warm") material, for which there is a substantial bound-free opacity (§ 4.4). Such cool/warm material can include both the ambient stellar winds (which are generally kept at temperatures near the stellar effective temperature—typically 30–60 kK—by the photoionization heating from the stellar UV flux), as well as the radiatively cooled material of the shocked interface itself.

For both these sources, we generally adopt an energy-dependent opacity κ_E appropriate for "warm" material, as detailed in § 4.4. This is then multiplied by an integral column depth from the X-ray source at each front location, thus giving the total optical depth $\tau_{\boldsymbol{m}}$ to an observer in some direction $\boldsymbol{m}$. For the cooled material in the compressed front, finding the associated column depth requires an analysis of the material transport along the front, as outlined in § 4.3 and further detailed in the Appendix. For the wind component, computing the column depths entails straightforward ray integrals over the local density $\rho = \dot{M}/4\pi v r^2$, as set by the wind mass-loss rate $\dot{M}$, speed $\boldsymbol{v}$, and distance r from its central star. However, note that, except for an observer direction along the x-axis ($\boldsymbol{m} = \pm\boldsymbol{x}$), this mass column will in general be a function of an azimuthal angle ψ around the x-axis, as well as the off-axis coordinate distance y.

Once optical depths $\tau_{\boldsymbol{m}}(y, \psi)$ are available for a full set of locations y, ψ of the front emitting surface, the flux spectrum detected by an observer at very great distance R in a given direction $\boldsymbol{m}$ can be determined by a generalization of equation (25),

$$F(E, \boldsymbol{m}) = \frac{1}{4\pi R^2} \int_0^{2\pi} \int_0^\infty \frac{S(y, E) e^{-\tau_{\boldsymbol{m}}(y,\psi,E)}}{\sin\phi} y\, dy\, d\psi z. \quad (26)$$

4.3. *Surface Density of Interaction Layer*

To account for the absorption from cooled material within the front interaction layer, we need to model the net accumulation of mass within this layer. The net local surface density at the interaction front is set by balance between the incoming mass flux *perpendicular* to the front and the subsequent transport of this material *parallel* to the front. In principal the flow parallel to the front should be determined from the full momentum balance, including gas-pressure terms, integrated along the front; but, as a more tractable approximation, we simply assume here that the parallel speed *within* the interaction layer is locally just equal to the corresponding parallel wind velocity component *outside* this layer.

Note that this approximation means that there may be shear between the two layers on either side of the contact discontinuity. Physically this shear layer would generate instabilities. However, since we assume no mixing, our model remains self-consistent. Canto et al. (1996) presented a formula for the surface density of a fully mixed radiative interaction layer. However, we cannot use it as we assume no mixing; also they only considered a constant wind speed case while we allow for β velocity laws.

To illustrate our basic approach let us consider here the simple case of equal wind momenta ($\eta = 1$), so that the interaction front is planar at the midpoint between the stars, i.e., $x = D/2$. And let us further assume that this distance is far enough that the winds speeds have reached their terminal value v_∞ (assumed for simplicity to be equal for both winds). (The Appendix gives a more complete, but rather technical, analysis of the general case with asymmetric, non–terminal-speed winds, including the effects of both front curvature and flow acceleration.)

For convenience, we adopt coordinates centered on star 1 (see Fig. 1), but to simplify notation, we omit any explicit subscripts 1, 2, since by symmetry, the same analysis applies to both winds.

Consider first the mass column at the very front of the interaction layer, i.e., along the x-axis, line-of-centers between the two stars. Since this is a symmetry axis, the y-component of the velocity must vanish, and this makes it a bit subtle to see how mass is removed from the axis. Our approach is to consider a small circular patch perpendicular to the x-axis, with radius dy and surface area $\pi(dy)^2$. The mass coming into the patch is ρv times this area, where ρ and v are the incoming wind density and velocity at the interaction layer, i.e., a distance $x = x_0 = D/2$ from the source star. The mass flux out of this patch is through the outer rim, given by the mass column σ_0 times the rim circumference $2\pi\, dy$, times the y-velocity at the outer rim. But by assumption the latter is just given by $v_y = v\, dy/x$, and so mass balance in this patch requires

$$\rho v \pi (dy)^2 = 2\pi\, dy\, \sigma_0 v\, dy/x, \tag{27}$$

which thus gives

$$\sigma_0 = \rho x/2 = \frac{\dot{M}}{4\pi \mathrm{v} D}. \tag{28}$$

This shows that the characteristic scale of the *front* surface density is roughly equal to source *wind* column density over the distance of the binary separation.

The surface density along the full interaction front follows from a similar analysis of mass balance within each differential ring segment of width dy centered at radius y from the x-axis. In this case, the x-direction wind mass flux over the ring circumference $2\pi y$ is balanced by the *difference* in the y-direction mass flux between the inner and outer edge of the ring

$$\rho v_x 2\pi y\, dy = d(\sigma v_y 2\pi y). \tag{29}$$

We again make the assumption that the velocities are just given by the projected components of wind velocity, i.e., $v_x = vx/r$ and $v_y = vy/r$, with the radius $r = (x^2 + y^2)^{1/2}$. After some manipulation, and using the definition in equation (28) of the x-axis surface density σ_0, equation (29) yields a differential equation for the y-variation of the surface density $\sigma(y)$

$$y\frac{d\sigma}{dy} = \frac{2\sigma_0 + \sigma(y/x)^2}{1 + (y/x)^2} - 2\sigma. \tag{30}$$

Very near the x-axis, where $y \ll x$, expansion to order $(y/x)^2$ gives equation (30) the form

$$y\frac{d\sigma}{dy} \simeq -\sigma_0 (y/x)^2 - 2y\frac{d\sigma}{dy}. \tag{31}$$

The vanishing of $d\sigma/dy \sim y$ means the mass density is roughly constant very near the x-axis, with the added mass from the wind just balanced by the cylindrical expansion of the y-direction outflow. Integration of equation (31) shows in fact that the variation is quadratic in (y/x),

$$\sigma(y) \simeq \sigma_0 \left(1 - \frac{y^2}{6x^2}\right);\ y \ll x. \tag{32}$$

In the opposite limit far from the axis, $y \gg x$, the wind mass flux becomes nearly parallel to the surface, implying its addition to surface density becomes negligible. The variation thus asymptotically approaches the form

$$y\frac{d\sigma}{dy} \simeq -\sigma, \tag{33}$$

which implies the surface density declines as the inverse of distance, owing to the cylindrical expansion

$$\sigma(y) \sim 1/r;\ y \gg x. \tag{34}$$

The general, asymmetric case with a curved interaction front and nonterminal wind speeds is analyzed in the Appendix. Results are plotted in Figure 11. The solid curves are for the symmetric wind case but also include the effects of nonterminal wind speeds. The decline in wind density with the radially increasing flow speed makes the axial decline of front surface density slightly steeper than the constant-speed model.

If we define $\boldsymbol{n}$ to be the outward normal of the local surface from a given cooling layer, then for an observer in direction $\boldsymbol{m}$, with $\boldsymbol{m}\cdot\boldsymbol{m} \geq 0$, the local surface increment of optical depth for the radiation emitted from that layer is

$$\Delta\tau_{\boldsymbol{m}}(y, E) = \frac{\kappa_E \sigma(y)}{\boldsymbol{m}\cdot\boldsymbol{n}}, \tag{35}$$

where κ_E is the absorption opacity for the photon energy E. This is combined with the corresponding increment from the cooling layer on the opposite side of the front, plus the integral optical depth from the wind, to give the total optical depth $\tau_{\boldsymbol{m}}$.

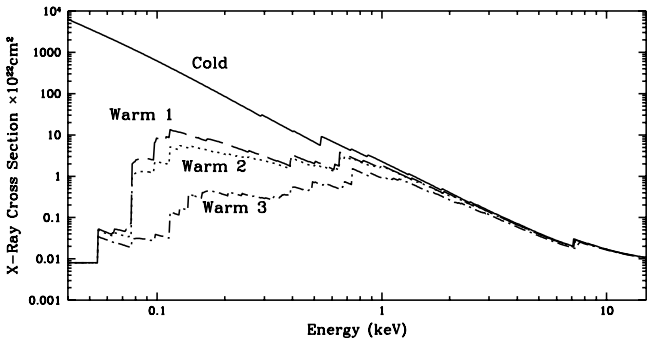

FIG. 5.—Absorption cross section for cold and warm medium. This is proportional to the opacity, or mass-absorption coefficient, κ_E. See the text for further comments. [*See the electronic edition of the Journal for a color version of this figure.*]

That then determines the attenuation of the local emission to the observer, as described in § 4.2 by equation (26).

4.4. *Absorption Opacity of "Warm" Material*

Let us now turn to determining the absorption opacity κ_E of the material in both the wind and the interaction layer. Because of the photoionization and associated heating of the bright stellar UV sources, both the wind and interaction layer should tend to have an opacity characteristic of "warm" material. This can differ significantly from the standard "cold" material opacity commonly used to estimate interstellar absorption, because the higher temperature implies a higher overall ionization state and thus reduced bound-free absorption. In the case of colliding winds, the ionization can be further enhanced by photoionization from shock radiation at the interaction front. In addition, for winds from a WR component the abundance can also differ from the standard "cosmic" values.

Such distinctions in opacity between a warm and cold medium were demonstrated by Waldron et al. (1998, see their Fig. 2), who found there can be significant reductions below 1 keV. Actually, in this as well as traditional interstellar studies, absorption properties are nominally characterized in terms of a medium-averaged *cross section*, normalized per hydrogen atom, and thus with units of area, i.e., cm^2. Thus, to facilitate comparison of results here with those of Waldron et al. (1998) and other studies, the plots here are likewise in terms of such a cross section. Conversion to opacity κ_E, with units $\mathrm{cm}^2\ \mathrm{g}^{-1}$, is then simply of matter of multiplying this cross section by $X_{\rm H}/(\bar{\mu} m_p)$, where $X_{\rm H}$ is the hydrogen number fraction, $\bar{\mu}$ is the mean atomic weight of the nuclei, and $m_p = 1.67 \times 10^{-24}$ g is the proton mass (see § 3.2.)

To compute the absorption cross sections for our models, we use the Cloudy version 94.00 code (van Hoof et al. 2000).[6] This code allows one to calculate ionization state, cross sections, and emission spectrum of a gas cloud, specifying the spectrum and intensity of the illuminating source, its distance to the gas cloud, and the cloud density and chemical abundances.

Figure 5 compares results for various conditions, for now assuming solar abundances. In all cases, we fix the distance from the central source at $r = 10^{12}$ cm and the hydrogen number density of the cloud at $n_{\rm H} = 10^{10}\ \mathrm{cm}^{-3}$, which are representative of a typical point in the wind models considered here. The solid line compares results for a cold medium, computed by setting the stellar luminosity to zero; except for the minor differences from the assumed abundance, this is very similar to standard cross section assumed for interstellar absorption.

The dashed line (labeled "warm 1" in Fig. 5) shows the cross section for the case with a stellar blackbody appropriate for typical O-type star, $T = 42,500$ K, $L_{\rm bol} = 1.5 \times 10^{39}$ ergs s^{-1}. The density of the cloud is taken to be constant, and its width is set 100 times smaller than r to suppress any radial dependence. This case represents a typical example of absorption cross section of a warm medium heated by a central hot star.

To examine how X-ray radiation affects the absorption cross section, Figure 5 also includes two more models with a bremstrahlung component added to the central illuminating source. The temperature of this component is set to $\log T_x = 7.5$. Its luminosity is 10^{34} ergs s^{-1} for the dotted line labeled "warm 2" and 10^{35} ergs s^{-1} for the dot-dashed line labeled "warm 3." The reduction in absorption is quite strong for the latter, but quite modest for the former. Although the typical bolometric luminosity of the wind-wind collision area can indeed range up to 10^{35} ergs s^{-1}, cooling models show that, even for strong shocks, the bulk this radiation is relatively soft ($\leq$0.5 keV), emitted from material at temperatures well below $10^{7.5}$ K. As such, the warm-2 model generally represents a more realistic example for high-temperature emission. Overall, it thus seems that, while X-ray radiation from the wind collision area can influence the ionization state and the optical depth of the winds, the overall effect is likely to be relatively modest. For the present study, we thus typically employ the warm-1 opacities, leaving further investigation of this issue to future work.

Figure 6 compares the cross sections at several distances from the sample star above, using the local radiation and wind densities at each distance for the O-type stellar and wind parameters: $\dot{M} = 10^{-6}\ M_\odot\ \mathrm{yr}^{-1}$, a velocity law with exponent $\beta = 1$, and $v_\infty = 2000\ \mathrm{km\ s}^{-1}$. Note that cross sections do not differ much, at least in the energy range of interest for X-ray observations. (*Chandra* or *XMM-Newton* are sensitive starting from ~0.2 keV.) This is because, while the stellar radiation becomes more diluted with increasing distance, so does the wind density. As a result, the ionization state of the wind material does not change dramatically.

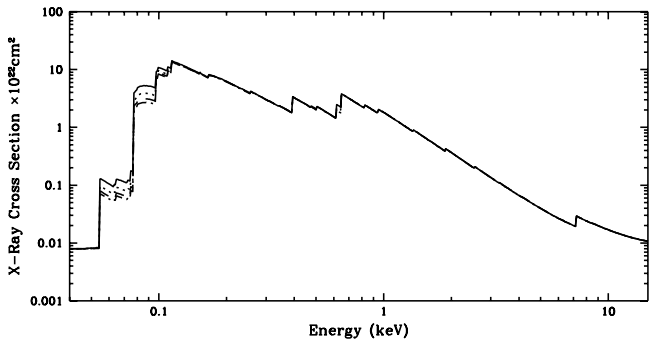

FIG. 6.—Dependence of the absorption cross section on the distance from a typical O star. *Solid line:* $r = 15\ R_\odot$; *dotted line:* $r = 20\ R_\odot$; *dashed line:* $r = 30\ R_\odot$; *dot-dashed line:* $r = 50\ R_\odot$. With increasing distance from the star the cross sections at low energies slowly decrease. [*See the electronic edition of the Journal for a color version of this figure.*]

[6] See http://thunder.pa.uky.edu/cloudy.

Overall, the above results suggest that, to account for the absorption of the X-ray radiation by both cooling layers and the stellar winds, we can reasonably use a common absorption cross section, computed for a typical point in that wind, taking the best available estimates for the stellar temperature and wind parameters for the relevant star. Of course within the cooling layers, the material immediately behind the shock is very hot and its absorption is greatly reduced. Thus, taking the surface density of the cooling layer derived in the previous subsection and a single "warm" absorption coefficient, we overestimate absorption by this hot component of the cooling layers. However, as the mass fraction of the hot material is relatively small and the whole method of accounting for the absorption is very approximate, we neglect this effect, leaving more accurate treatment of the absorption for the future work.

5. SIMULATED MODELS: INTRINSIC PROPERTIES

Before presenting detailed results for X-ray spectra, let us first review some of the general intrinsic properties of the associated wind-collision models.

5.1. *Interaction Front and Cooling Layers*

Figure 7 illustrates the contact surfaces for different values of η, each labeled with the corresponding model parameters. Note that the values of η_0 at the shock apex ($y = 0$) are significantly different from the values η_∞ obtained by using the terminal velocities in equation (3). This is because the system is relatively close and the wind velocities at the position of the interaction front have not yet reached their terminal values.

Another consequence of this inclusion of wind acceleration is that it becomes impossible to maintain momentum balance at a contact surface very close to the surface of the secondary star. With the parameters used, $\dot{M}_2 = 0.26 \times 10^{-6}\ M_\odot\ \mathrm{yr}^{-1}$ is about the minimum secondary-component mass-loss that still maintains a momentum balance somewhere between the stars. Below this value the momentum of the primary wind is larger than the momentum of the secondary one, at any position x. This is illustrated in Figure 8, which plots the momenta of the two winds for the model with the smallest η. One can see that the momentum of the secondary wind (*dashed line*) barely reaches the momentum of the primary one. Still the position of the equilibrium point is quite far from the secondary star. This is again because in the assumed β-law form for the velocity, the secondary wind needs some distance to gain speed and reach its maximum momentum flux density.

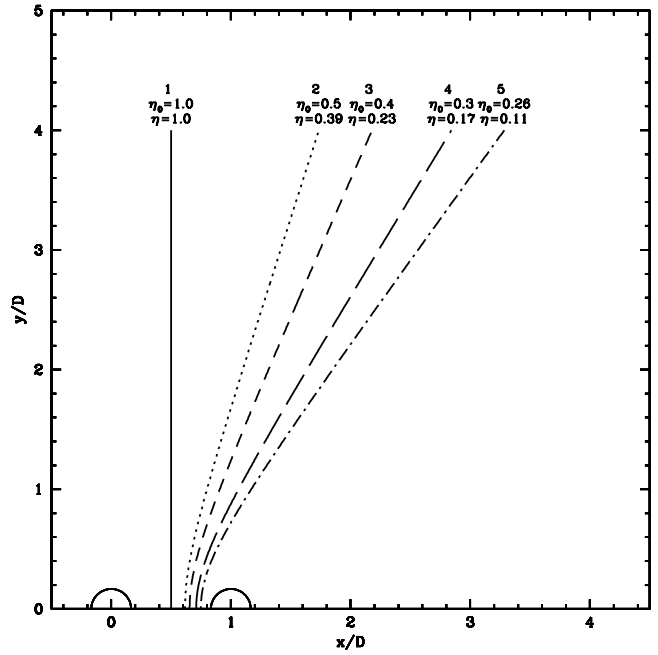

FIG. 7.—A few examples of contact surfaces. The labels show the values of η_0 at the shock apex $y = 0$, with velocities in eq. (3) taken from the wind velocity laws, while the η_∞ use the terminal velocities in eq. (3). The parameters of the models are the distance between the components $D = 60\ R_\odot$, $r_{*1} = r_{*2} = 10\ R_\odot$, $V_{1,\infty} = V_{2,\infty} = 2000$ km s^{-1}, $\beta_1 = \beta_2 = 1$, $\dot{M}_1 = 1.0 \times 10^{-6}\ M_\odot\ \mathrm{yr}^{-1}$, and $\dot{M}_2 = 1.0$, 0.5, 0.4, 0.3, $0.26 \times 10^{-6}\ M_\odot\ \mathrm{yr}^{-1}$ for the models 1–5, respectively. [*See the electronic edition of the Journal for a color version of this figure.*]

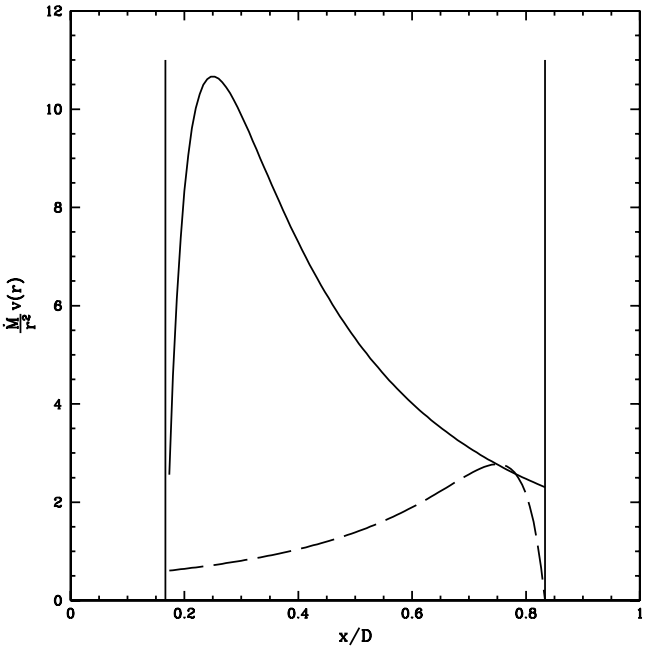

FIG. 8.—Wind momenta for model 5 of the previous plot. *Solid line:* primary wind; *dashed line:* secondary wind. Stellar radii are shown by the vertical lines. [*See the electronic edition of the Journal for a color version of this figure.*]

For model 3 from Figure 7, the additional plots in Figures 9 and 10 illustrate several characteristics of the interaction zone. The parameters of this model represent a typical, relatively close O+O binary system, in which we expect the shocks to be radiative. Figure 9 shows the normal and tangential velocities of the primary wind. Figure 10 illustrates the narrow, but finite-width of the cooling layers.

5.2. *Surface Densities of the Cooling Layers*

For the same models as in Figure 7, Figure 11 shows the surface density distributions along the contact surface for the two cooling layers. Some noteworthy aspects this plot are the following:

1. With decreasing η, the surface density of the primary cooling layer decreases, since the distance of the shock from the primary star is increasing.

2. Effects are somewhat subtler for the surface density from the secondary star. As η is decreased, the shift of the interaction front toward the secondary star increases its associated wind density, which thus increases its front surface density at or near the x-axis. But the decreased η also increases the front curvature, tilting the surface to a more parallel orientation to the flow

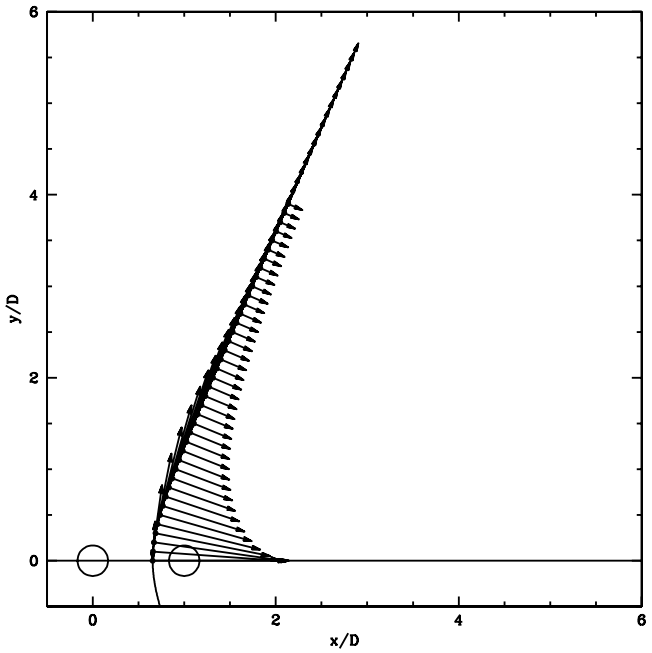

FIG. 9.—Normal and tangential velocities of the primary wind at the interaction front, for the model 3 from Fig. 7. The dots show the grid points on the contact surface. The actual grid is much denser, but we skipped many grid points to avoid crowding the plot. [*See the electronic edition of the Journal for a color version of this figure.*]

velocity. The reduced incoming normal mass flux thus leads to a sharper axial decrease in surface density.

3. At any given y, the surface density of the secondary cooling layer is always either equal to or larger than that of the primary one. This is again because the front is closer to the secondary star than to the primary; Since its wind velocity at the shock position is smaller (recall that in these models the v_∞ and β of both winds are identical), maintaining momentum balance requires having a larger local wind density and, consequently, a denser cooling surface.

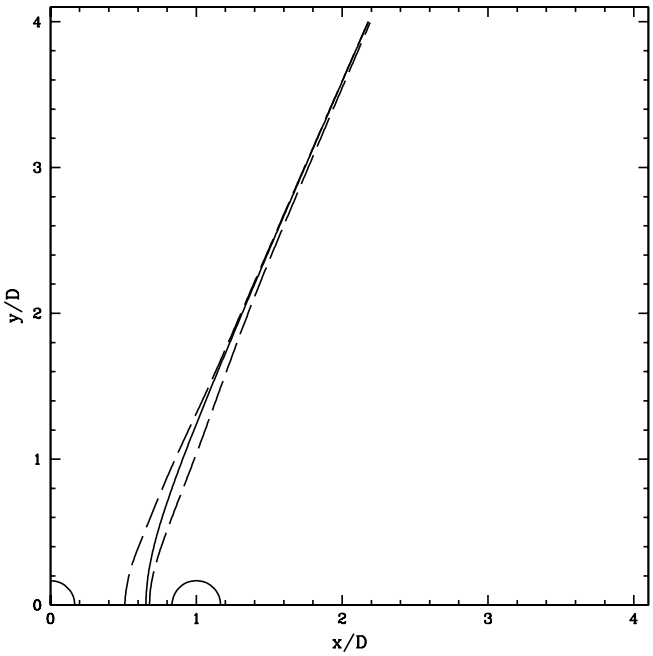

FIG. 10.—Width of the cooling layers for model 3. The solid line represents the interaction front; the dashed lines represent shock edges. The width of the cooling layer along the line connecting the components is $dl_1 = 0.146D$ for the primary star and $dl_2 = 0.025D$ for the secondary. [*See the electronic edition of the Journal for a color version of this figure.*]

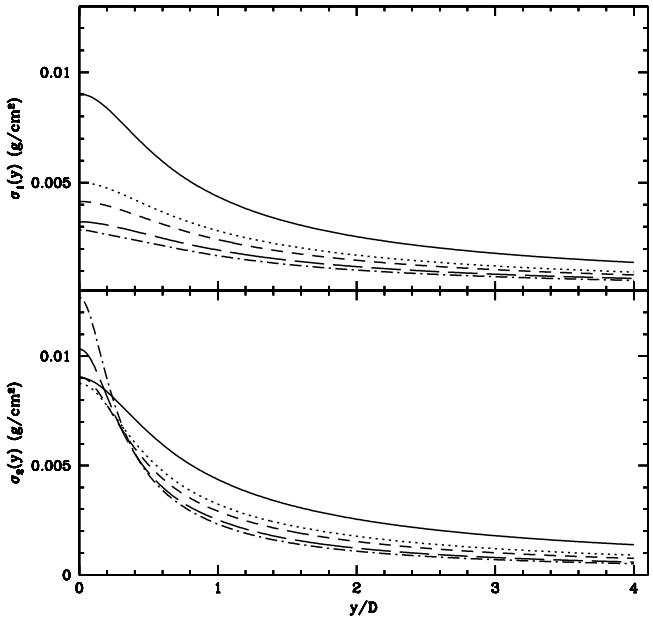

FIG. 11.—Surface density of the cooling layers along the contact surface for the models from fig. 7. *Solid line:* 1; *dotted line:* 2; *short-dashed line:* 3; *long-dashed line:* 4; *dot-dashed line:* 5. [*See the electronic edition of the Journal for a color version of this figure.*]

5.3. *The Kinetic Energy Released at the Interaction Front and the Intrinsic X-Ray Spectra*

The kinetic energy of the two winds provides the energy for the shock emission and so sets the total luminosity of the emission. The hardness of the emitted spectra, on the other hand, is set by the velocity component normal to the front, which defines the specific energy and thus the immediate postshock temperature. It is therefore instructive to examine how the specific and total kinetic energy associated with the front-normal wind component depends on the position along the contact surface.

For model 3, the top panel of Figure 12 plots the immediate postshock temperatures of the two winds as a function of the y-coordinate. In this particular model, the primary wind dominates the intrinsic X-ray emission. As expected, the highest temperatures (thus the hardest spectra) occur near $y \simeq 0$, where the normal components of the wind velocities are maximal. The bottom plot shows the kinetic energy carried per second through a circular strip of the interaction front (the width of the strip is taken to be $dy = 0.01d$), again for the two winds, as a function of the immediate postshock temperature. The maxima of these functions roughly give the energy at which the bulk of X-ray emission is emitted. These results are similar to those of Pittard & Stevens (2002). Figure 13 compares the hardness of the intrinsic X-ray spectra produced at sections of the interaction zone near to and away from the x-axis.

6. SIMULATED SPECTRA FOR CHARACTERISTIC BINARY PARAMETERS

We now present emitted spectra from our model simulations for various configurations of a colliding wind binary. The

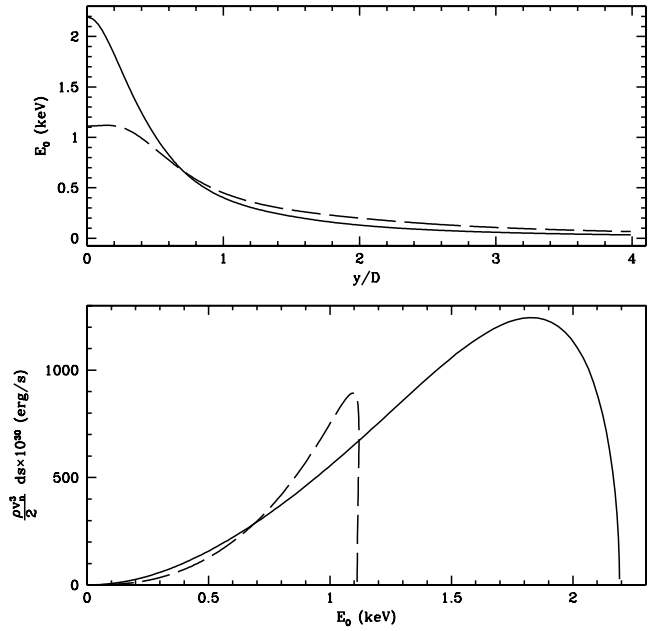

FIG. 12.—Model 3. *Top:* The immediate postshock temperature vs. *y*. *Bottom:* The kinetic energy of the winds (*solid line:* primary wind; *dashed line:* secondary wind) entering a given circular strip ($dy = 0.01D$) on the contact surface per second, plotted vs. the immediate postshock temperature of the strip. [*See the electronic edition of the Journal for a color version of this figure*.]

models here are meant to representative of massive binaries but do not correspond in detail to any particular system. Readers interested in seeing an example of application of the method to a specific X-ray data set are referred to De Becker et al. (2002).

First, to compute X-ray spectra from the collision area at different orbital phases of a binary system, we must specify an orbital model. In the general case of an eccentric orbit, our set of orbital parameters includes the orbital inclination i, semimajor axis a, eccentricity e, and the longitude of the periastron ω. Figure 14 illustrates the orbital geometry. The relations among various parameters describing orbital motion (e.g., true and mean anomaly, current distance between the components D, etc.) can be found in standard textbooks on celestial mechanics and will not be presented here. It is perhaps worth

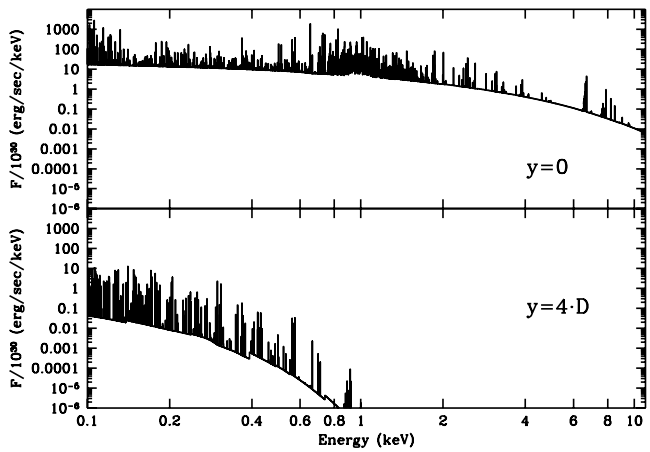

FIG. 13.—Intrinsic X-ray spectra of two surface strips for the primary cooling layer. *Top:* at $y = 0$; *bottom:* at $y/D = 4$.

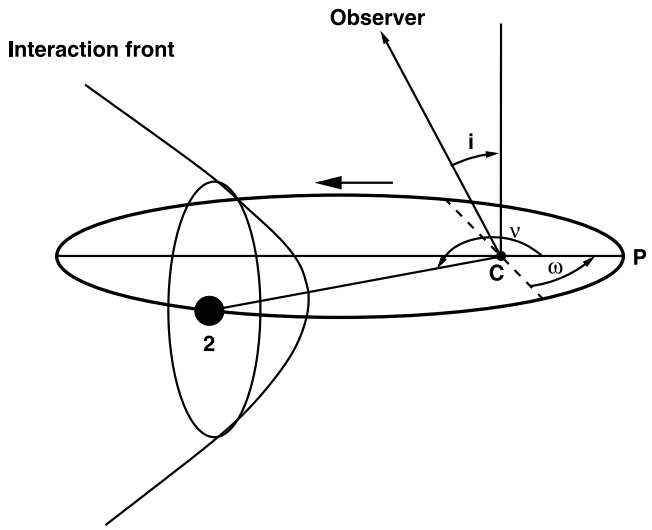

FIG. 14.—Illustration of the orbital model used in this study (only the orbit of the secondary star is shown). The vertical line is normal to the orbital plane. The dashed line is the intersection of the orbital plane and the plane of the sky (and is perpendicular to the line of sight shown as the line from C to observer); i is orbital inclination, ν is the true anomaly, P marks the periastron, and C marks the center of mass.

emphasizing that our neglect of the orbital motion in computing the shape of the interaction front means that in our models this front instantly follows the orbital motion of the component stars. Here we define zero orbital phase to be at periastron passage.

To isolate the effects of the binary separation, wind opacity, chemical abundances, and the strength of the winds, we compute X-ray spectra and light curves for a series of simple models, with parameters summarized in Table 1. In all cases but one we set the orbital inclination $i = 90^{\circ}$ to maximize orbital modulation effects.

6.1. *Model A*

For our first model, let us consider the simple case of a circular orbit system with identical stars and winds. In this case, phase zero is an eclipse phase, with component number 2 being in front. Figure 15 plots the light curve of this model in the energy range 0.5–10.0 keV. Note that, as to be expected for this highly symmetric system, the light curve shows dual symmetry about phases corresponding to both quadrature (0.25, 0.75) and alignment (0, 0.5) of the stars to the line of sight. The minimum of the luminosity occurs at the alignment phases 0.0 and 0.5, when the brightness emitting region between the stars is subject to the greatest attenuation by stellar occultation and wind absorption. As orbital phase increases to 0.25, the line of sight to this bright region passes through less dense parts of the stellar wind, with little or no stellar occultation, and so the brightness increases. The narrow, deep dip very near phase 0.25 is due to the absorption from the geometrically thin layer of cooled gas at the interaction front. In real systems any such dip is likely to be broader and more shallow, owing to the finite extension of the cooling front, which may be additionally broadened by various front instabilities (Stevens et al. 1992; Vishniac 1994; Walder & Folini 2000).

Figure 16 compares the spectra of model A at phases 0.0 (minimum L_X) and 0.2 (maximum L_X). For comparison, the

TABLE 1
STELLAR, WIND, AND ORBITAL PARAMETERS OF THE SIMULATED MODELS

PARAMETER	VALUE	
	Star 1 (10.0 $R_\odot$)	Star 2 (10.0 $R_\odot$)
Model A		
i (deg)	90.0	90.0
e	0.0	0.0
$\dot{M}$ (10^{-6} $M_\odot$ yr^{-1})	1.0	1.0
V_∞ (km s^{-1})	2000.0	2000.0
β	1.0	1.0
Model A Variant 1		
β	0.5	0.5
Model B		
i (deg)	90.0	90.0
e	0.0	0.0
$\dot{M}$ (10^{-6} $M_\odot$ yr^{-1})	1.0	0.5
V_∞ (km s^{-1})	2000.0	2000.0
β	1.0	1.0
Model C		
i (deg)	90.0	90.0
e	0.4	0.4
$\dot{M}$ (10^{-6} M yr^{-1})	1.0	1.0
V_∞ (km s^{-1})	2000.0	2000.0
β	1.0	1.0
Model C Variant 1		
V_∞ (km s^{-1})	1000.0	1000.0
β	0.0	0.0
Model C Variant 2		
i (deg)	45.0	

For the assumed semimajor axis $a = 60$ $R_\odot$; $\omega = 270.0$. and $R_* = 10.0$ $R_\odot$. Kepler's third law implies orbital periods and stellar masses related by $P = 15.6$ day $[20M_\odot/(M_1 + M_2)]^{1/2}$.

intrinsic unabsorbed spectra are also shown (the higher intensity functions on the plots). The decrease of the wind absorption in the soft part of the spectra toward phase 0.2 is evident. Note that the lower intensity of the hard part of the spectrum at phase 0.0 is not due to larger wind absorption but mainly results from stellar occultation of the part of the interaction front near the system axis, which is the main source of the hard X-rays.

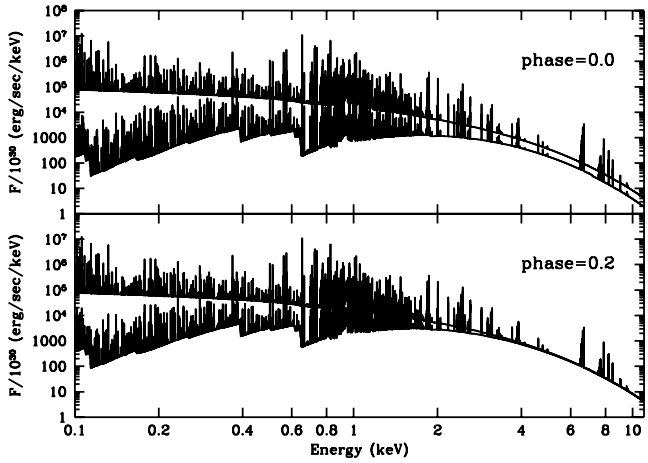

FIG. 16.—Intrinsic and absorbed spectra in model A at two orbital phases. [*See the electronic edition of the Journal for a color version of this figure.*]

We also computed a variant of model A with velocity exponent $\beta = 0.5$ for both winds, but we do not show the light curves and the spectra, since they are qualitatively very similar to the main model A. The main difference is that the X-ray luminosity is about 50% larger at all orbital phases; this is evidently due to the fact that $\beta = 0.5$ results in faster acceleration and thus makes available increased kinetic power for conversion into X-ray radiation.

6.2. *Model B*

Our second model is similar to the first, except that the secondary mass-loss rate is reduced by a factor of 2. Figure 17 shows that the light curve is again symmetric about the aligned phases (0, 0.5), but the different wind strengths lead now to some asymmetry relative to quadrature phases (0.25, 0.75). At phase 0.0 the secondary star is in front. Additional differences from model A include the following:

1. The luminosity at phase 0.0 is higher than at 0.5, since the wind of the secondary component is less dense and thus less opaque.
2. The phase of the sharp decrease of the luminosity is not exactly at 0.25, as in model A. The position of the minimum corresponds to the phase when the line of sight is tangent to the part of the interaction front, which produces the bulk of the emission. Also, the luminosity at this phase is not zero since the interaction front is curved and there are always some parts of it nontangent to the line of sight.

Figure 18 shows spectra of model B at three characteristic phases. The general properties of the spectra are qualitatively

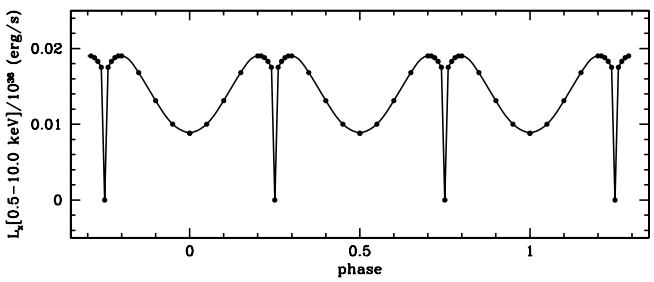

FIG. 15.—Light curve of model A. At phase 0.0 both stars are aligned in the line of sight.

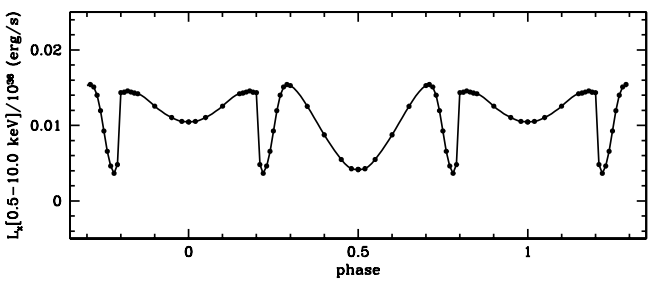

FIG. 17.—Light curve of model B. At phase 0.0 the secondary component is in front.

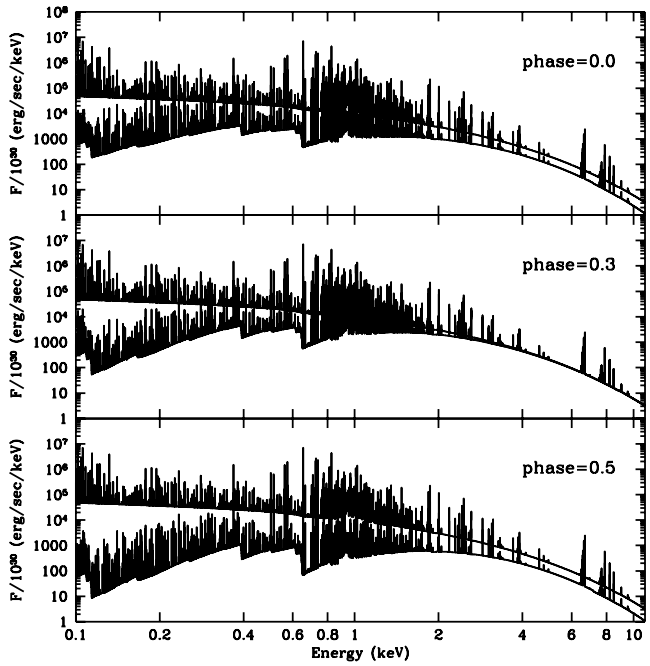

FIG. 18.—Intrinsic and absorbed spectra in model B at 3 orbital phases 0.0 (the secondary component in front), 0.3 (maximum L_X), and 0.5. [*See the electronic edition of the Journal for a color version of this figure.*]

similar to those of model A. Note the slightly weaker hard-tail intensities at phase 0.5 than at phase 0.0. This shows that, in addition to the geometrical occultation of the near-axis part of the interaction front, some relatively small wind absorption also acts in the denser wind.

Our light curves for models A and B are qualitatively similar to those of Pittard & Stevens (1997, see their Figs. 3 and 6).

6.3. *Model C*

This model illustrates the effects of the changing orbital separation on the X-ray spectra and light curve. Note that at apastron, our radiative assumption is somewhat "stretched." It is about as far as one could go with the present model. As we chose $\omega = 270^\circ$, the light curve shown in Figure 19 is symmetric relative to the phase 0.5 (at phase 0.0 the secondary star is in front). At a different ω it would be correspondingly shifted along the horizontal axis. At first sight, the behavior of the light curve may seem surprising. Quite often it is assumed that the X-ray luminosity of an eccentric colliding wind binary at periastron should be maximal, since the density of the colliding winds is the highest there.

In fact, this common conception is only valid for the case of adiabatic shocks and constant wind velocities. Luo et al. (1990) have shown that for the winds of similar strengths the X-ray luminosity in the adiabatic case scales as $L_X \propto \dot{M}^2 v^{-3.2} d^{-1}$. A similar result was obtained by Usov (1992), who derived an approximate formula for L_X, which, in the case of constant wind velocities, is inversely proportional to the distance between the components.

The situation can be quite different if, as in our model, the intrinsic X-ray luminosity is a more or less constant fraction of the wind kinetic power carried into the shock. This is easiest to see in the case of two equal winds and constant wind velocities. Since in this case the contact surface is a plane perpendicular to the system axis, we can analytically compute the amount of the wind kinetic power carried into the shock. Writing x as the distance from a star to the contact plane, v as the (constant) wind velocity, and $\dot{M}$ as the mass-loss rate, then the kinetic power entering the shock is

$$P_{\rm kin} = 2\pi \int_0^\infty \frac{\dot{M}}{4\pi r^2 v} \frac{v^3 \cos^3\theta}{2} p\, dp,$$

where $r = (x^2 + p^2)^{1/2}$, $\cos\theta = x/r$. It is easy to see that the integral is equal to $\dot{M}v^2/12$, and is constant and does not depend on the distance between the components. This conclusion is valid also for unequal winds, provided that their expansion velocities are constant. Indeed, in this case the geometry of the wind-wind collision is scale-free, so as long as the shocks still remain radiative, L_X should not depend on D. Luo's et al. relationship should be defined as the variation in the intrinsic X-ray luminosity in the adiabatic case.

In our model, which represents a relatively close binary system, two other factors play an important role: the spatial variation of the wind velocities, and the absorption of the intrinsic X-ray radiation in the cooling layers and in the winds. This becomes clear from the plots of the spectra at three characteristic phases: 0.0 (periastron), 0.25 (maximal luminosity), and 0.5 (apastron). This plot is consistent with the result of Pittard & Stevens (1997), who showed that wind absorption means that there is always a separation where the *observed* luminosity peaks (see their Fig.). The spectra are shown in Figure 20.

First, note that the *intrinsic* unabsorbed spectrum at periastron (*top*) is much softer than at the apastron (*bottom*). Its luminosity is also smaller, as illustrated in Figure 21. The reason is that the wind velocities at the interaction front are much smaller at periastron than at apastron. At phases 0.25 and 0.5 the velocities of the winds at the interaction front have nearly reached their terminal values, so the intrinsic spectra and their luminosities are very similar (see Figs. 20 and 21).

Now let's turn to the absorption of the X-ray spectrum. As in our previous models, the hard tail of the spectrum is occulted by the stars at periastron and apastron (Fig. 20, *top and bottom, respectively*). What is more interesting is that absorption of the soft part of the spectrum is much stronger at periastron than at apastron. This cannot be due to the absorption in the winds. A ray from a given point of the interaction front to the observer has exactly the same impact parameter at periastron or apastron. Since the stellar and wind parameters of both components are identical, the wind column densities should be similar, too. In fact, at apastron the column density should be larger since the ray travels longer in the

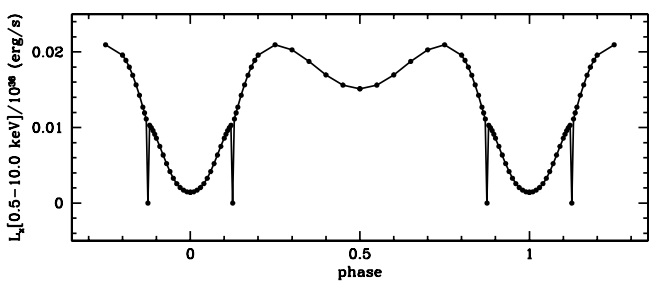

FIG. 19.—Light curve of model C. At phase 0.0 (periastron) the secondary component is in front.

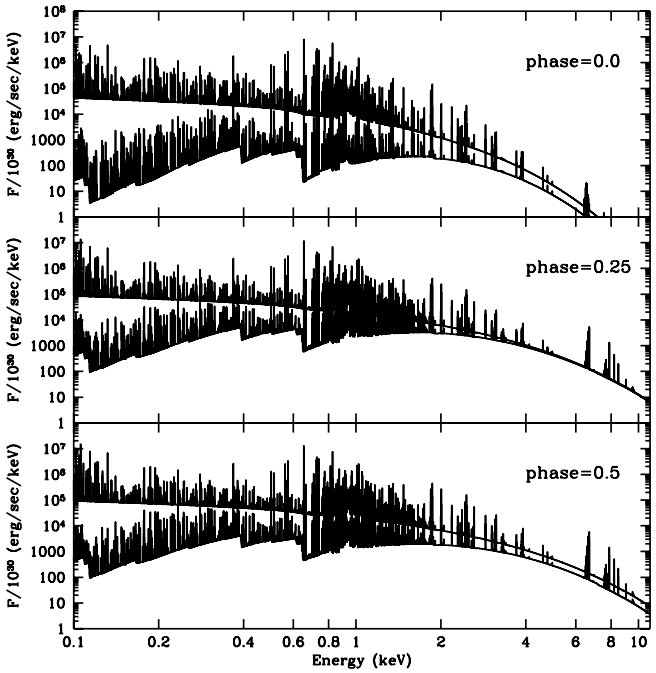

FIG. 20.—Intrinsic and absorbed spectra in model C at three orbital phases 0.0 (periastron, the secondary component in front), 0.25 (maximum L_X), and 0.5 (apastron). [*See the electronic edition of the Journal for a color version of this figure*.]

wind of the primary. The reason for larger absorption at periastron is that the column density of the cooling layers is higher than at the apastron. Thus, it is this absorption *within* the cooling layers that makes the difference between soft absorption at periastron and apastron.

To illustrate such issues further, let us consider a variant of model C in which all stellar, wind, and orbital parameters are the same but the velocities of the two winds are constant and fixed at 1000 km s^{-1} (at 2000 km s^{-1} the thin shell approximation for the cooling layers brakes down). The intrinsic, unabsorbed X-ray luminosity is indeed constant, as discussed above (and thus not shown here). The light curve (Fig. 22) now reflects changing absorption and occultation in the cooling layers and the winds. This is also evident from the plot of the spectra (Fig. 23). The intrinsic spectra at all phases are identical, while the absorbed spectra are similar to those of the main model C.

Figure 24 shows the light curve of another variant of model C, in which the inclination angle is decreased to $i = 45^{\circ}$. This clearly demonstrates the effect of decreased absorption. The effect is more pronounced at apastron, since geometrical occultation of the most luminous part of the

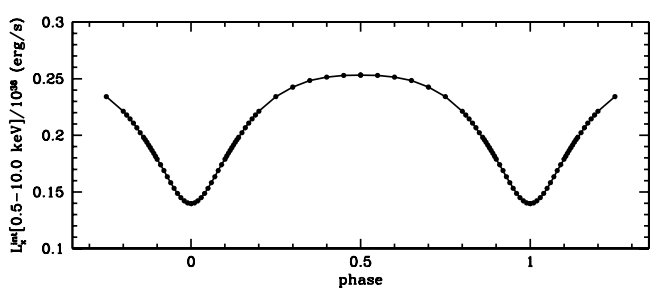

FIG. 21.—Intrinsic (unabsorbed and unocculted) luminosity in model C.

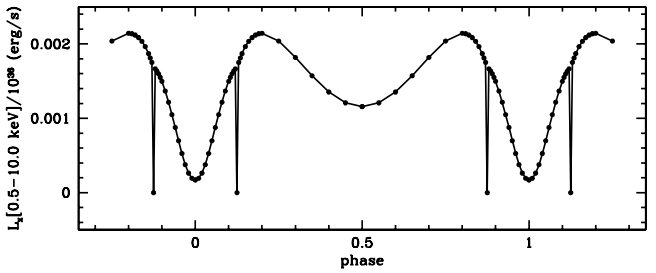

FIG. 22.—Light curve of a variant of model C with constant wind velocities. In comparison to Fig. 19 the maximum L_X is reduced since the slower wind speeds mean that there is less kinetic power and more absorption for given mass-loss rates.

interaction front near the system axis is much smaller than at the periastron.

7. XSPEC ANALYSIS OF A SIMULATED MODEL

It is of interest to analyze simulated model spectra with a standard tool like XSPEC, to explore how the plasma parameters obtained with this tool compare with the known properties of the model. For this purpose, we chose our model B.

First, to be able to use our model spectra in XSPEC, we create a so-called XSPEC table model. (This is a custom model that can then be used within XSPEC like any built-in model.) This model is then used within XSPEC to simulate an artificial data set, as if observed by the MOS1 *XMM-Newton* detector (Jansen et al. 2001). That is, our model spectra are convolved with the *XMM-Newton* response curves, Poisson statistics corresponding to a typical exposure time of 20 Ks is added, etc. Second, this simulated data set is read into XSPEC and analyzed in a standard way. To perform this analysis, we select the simulated spectrum in model B at the orbital phase 0.3 (maximum X-ray luminosity). The reason is that at this phase the most luminous parts of the interaction zone is not occulted by

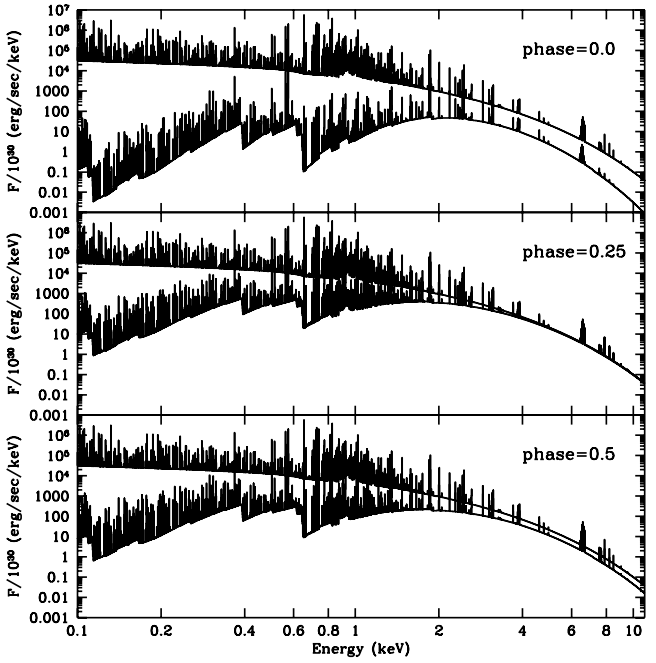

FIG. 23.—Intrinsic and absorbed spectra in a variant of model C with constant wind velocities. [*See the electronic edition of the Journal for a color version of this figure*.]

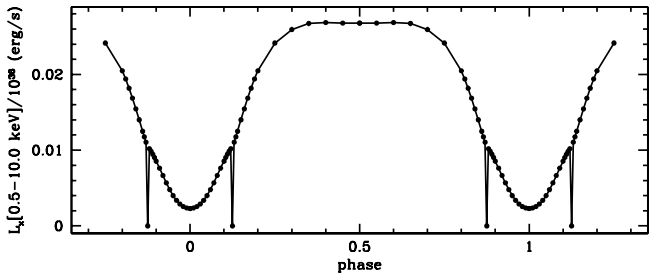

FIG. 24.—Light curve of a variant of model C with inclination angle $i = 45^{\circ}$.

the star bodies (which could create additional complications when comparing the XSPEC results with our model).

Unsurprisingly, a one-temperature model is unable to achieve a good fit of the data. A better fit is obtained with the combination of XSPEC additive and multiplicative models WABS*MEKAL+WABS*MEKAL, where WABS is a model for the interstellar medium absorption and MEKAL is a model of thermal optically thin plasma (we used solar abundances). This two-temperature fit and its best parameters are shown in Figure 25 and in Table 2. The reduced $\chi^2 = 4.2$, which makes the fit still unacceptable. From Figure 25 it is clear that the main difference between the XSPEC model and the simulated data occurs in the soft part of the spectrum. One could add more components to the XSPEC model, but this seems unwarranted for our illustrative example.

Interestingly, in the XSPEC fit, the hydrogen column density for the hard component of the spectrum is quite large, while it is equal to zero for the soft component. The value of $N_2^{\rm H}$ is also quite unrealistic for our particular simulated system. The characteristic hydrogen column density in model B (from the apex of the contact surface toward the observer at phase 0.3) is equal to $N^{\rm H} = 0.19 \times 10^{22}$ cm^{-2}. These results illustrate the difficulties and ambiguities in using programs like XSPEC to infer physical parameters in systems like colliding-wind binaries.

8. CONCLUDING OUTLOOK

The approach described above provides a tractable, efficient way to derive X-ray emission spectra from the radiative shocks characteristic of wind-wind collisions in close, massive-star binaries. But to maintain perspective, let us summarize some

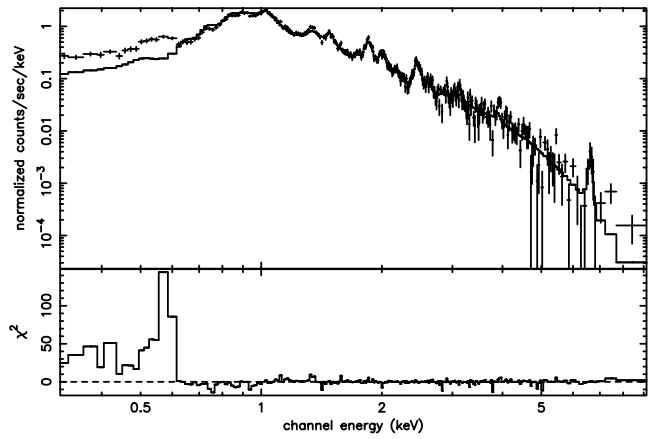

FIG. 25.—XSPEC fit of a simulated MOS1 *XMM-Newton data* for model B. The simulated spectrum corresponds to the orbital phase 0.3 when the X-ray luminosity is maximal.

TABLE 2
XSPEC FITTING OF MODEL B

Parameter	Value
$N_1^{\rm H}$ (cm^{-2}):	0.0
kT_1 (keV).....	0.65
Norm	1.42×10^{-3}
$N_2^{\rm H}$ (cm^{-2}):	0.89×10^{22}
kT_2 (kev)	1.11
Norm	1.00×10^{-2}

of the key approximations and limitations of the present implementation.

1. In neglecting an unknown physical level of mixing that may occur in radiative shocks, as well as adiabatic expansion, the derived spectra only define upper limits for the X-ray brightness and hardness for a given system.
2. The assumption of two-dimensional axisymmetry for the interaction front ignores the role of orbital motion in deflecting the larger scale front into a three-dimensional spiral form.
3. The treatment of absorption assumes a fixed, warm-medium opacity and does not account self-consistently for the effect of X-ray radiation in ionizing both wind and compressed front material.
4. The wind models assume fixed, kinematic velocity laws and so ignore effects like radiative inhibition (Stevens & Pollock 1994) or braking (Gayley et al. 1997) that depend on the dynamical role of the stellar radiation fields.

Future development may reduce these limitations. Item 1 is difficult to address on a fundamental level, but it might initially be accommodated in terms of some phenomenological mixing formalism. For item 2 the effect on X-ray emission from the region between the stars might be analyzed in terms of an perturbation approach, and ultimately even some three-dimensional spiral-cone model for the interaction front could be developed. Item 3 requires application of multidimensional radiative transfer methods (e.g., Whitney et al. 2003). Item 4 could be addressed by including the stellar radiation in the ram-pressure balance.

But even in the current configuration, the formalism developed here represents a substantial advance over previous approaches for interpreting X-ray emission from radiative shocks in cooling-wind systems. A principal result of the initial sample models computed here regards the broad, distinctive form of the emitted X-ray spectra. Because of the range of formation temperatures—both within a given shock cooling layer, and cumulatively over the differing shock strengths of the interaction front—the cumulative spectrum simply cannot be well fitted by the usual single- or even two-temperature thermal emission models of standard X-ray analysis packages like XSPEC (see § 7).

The method here is moreover quite computationally efficient, allowing iterative application to fit a specific observation set for given system. For example, for an initial application to the interpretation of *XMM-Newton* observations of the massive binary HD 159176 (De Becker et al. 2004), we generated a multiparameter grid of nearly 1000 models by running our code over just a few days on a standard workstation. This demonstrates a clear potential for further application to numerous recent and upcoming X-ray observations of close binaries of massive stars by both *XMM-Newton* and *Chandra*. At least in its current state, the code is too

specialized and complex for public posting as a standard analysis package. But we do intend to make it broadly available for analysis of such specific X-ray data sets.

We are grateful to J. M. Pittard for useful discussions and careful reading of the manuscript, as well as creating an XSPEC table model. I. I. A. acknowledges support from a PPARC grant and the Russian Foundation for Basic Research grant 02-02-17524. S. P. O. acknowledges support from NSF grant AST 00-97983 and NASA grants NAG5-11886 and NAG5-11095 at the University of Delaware, as well as a PPARC fellowship for a sabbatical visit to the University of Glasgow.

APPENDIX

CURVATURE AND ACCELERATION EFFECTS ON FRONT SURFACE-DENSITY

Here we generalize the analysis of § 4.3 to take account of the effects of front curvature and wind acceleration on the surface density in the interaction front. We again begin by considering a small circular patch at the x-axis, with radius dy and surface area $\pi(dy)^2$. For the front forming from star 1, the mass coming into the patch is $\rho_1 v_1$ times this area, where ρ_1 and v_1 are the incoming wind density and velocity at the interaction layer, i.e., at distance x_0 from the source star. The mass flux out of this patch is through the outer rim, given by the mass column $\sigma_1(0)$ times the rim circumference $2\pi\, dy$, times the tangential velocity at the outer rim. The last of these is given by

$$v_{1\|}(dy) \simeq v_{1\|}(0) + \left.\frac{dv_{1\|}}{dy}\right|_{y=0} dy = v_1 \left.\frac{d\cos\theta_1}{dy}\right|_{y=0} dy.$$

Thus steady mass balance in this patch requires

$$\rho_1 v_1 \pi(dy)^2 = 2\pi\, dy\, \sigma_1(0) v_1 \left.\frac{d\cos\theta_1}{dy}\right|_{y=0} dy.$$

For convenience, let us introduce the notation $z_0 \equiv d^2x/dy^2\,|_{y=0}$ and then write

$$\frac{dx}{dy} \simeq z_0\, dy;\ x \simeq x_0 + \frac{1}{2} z_0\, dy^2.$$

Noting from Figure 1 that $\cos\theta_1$ is the scalar product of the unit vectors in the direction of $\boldsymbol{r}_1$ and the tangential direction to the contact surface, we find

$$\cos\theta_1 = \cos\delta_1 \cos\phi + \sin\delta_1 \sin\phi. \tag{A1}$$

Expansion of each of these trigonometric functions to the first order in dy then yields

$$\frac{d\cos\theta_1}{dy} \simeq \frac{1 + z_0 x_0}{x_0},$$

which thus gives

$$\sigma_1(0) = \frac{\rho_1 x_0}{2(1 + z_0 x_0)}. \tag{A2}$$

Similar analysis of the second shock yields

$$\sigma_2(0) = \frac{\rho_2 (D - x_0)}{2[1 + z_0 (x_0 - D)]}. \tag{A3}$$

We can obtain z_0 by a straightforward but tedious analysis, the details of which we omit here. For the general case of variable wind speeds, the result is

$$z_0 = \frac{4(\sqrt{1 - \sqrt{\eta}})/\sqrt{\eta}/x_0 + x_0(c_1 - c_2)}{6 - x_0[c_1 x_0 + c_2 (D - x_0)]}, \tag{A4}$$

where

$$c_1 \equiv \frac{\beta_1/x_0^2}{(x_0/r_{*1}) - 1},$$

$$c_2 \equiv \frac{\beta_2/(D - x_0)^2}{(D - x_0/r_{*2}) - 1}.$$

In the case of constant wind expansion velocities (so that $\eta = \text{const}$, with β_1 and β_2, and thus c_1 and c_2, all vanishing), this simplifies to

$$z_0 = \frac{2\sqrt{1-\sqrt{\eta}}}{3x_0\sqrt{\eta}}. \tag{A5}$$

To compute the surface density along the full interaction front, we carry out a similar analysis of mass balance within each differential ring segment of height dy centered at radius y from the x-axis. In this case, the wind mass flux along the normal to a differential ring of width $dy/\sin\phi$ and circumference $2\pi y$ is balanced by the difference in the tangential mass flux between the inner and outer edge of the ring

$$\frac{\rho_1 v_{1\perp} 2\pi y\, dy}{\sin\phi} = d(\sigma_1 v_{1\parallel} 2\pi y). \tag{A6}$$

We again make the assumption that the velocities are just given by the projected components of wind velocity, i.e., $v_{1\perp} = v_1 \sin\theta_1$ and $v_{1\parallel} = v_1 \cos\theta_1$. Then if we define the auxiliary function

$$\xi_1 \equiv \sigma_1 v_1 \cos\theta_1 y,$$

we obtain the differential equation

$$\frac{d\xi_1}{dy} = \frac{\dot{M}_1 \sin\theta_1 y}{4\pi r_1^2 \sin\phi}. \tag{A7}$$

Given a solution of the interaction front geometry (§ 2), all the terms on the right-hand side are known functions of y. As such, straightforward numerical integration of equation (A7) from the x-axis ($y = 0$) yields the full variation along the front, $\xi_1(y)$, from which we can obtain the surface density via $\sigma_1 = \xi_1/(y v_1 \cos\theta_1)$.

Note however that $\xi_1(y \to 0) \to 0$, since both y and $\cos\theta_1$ vanish at the x-axis. This makes the determination of σ_1 singular at the axis, and so for very small $y \ll x_0$, it is best to obtain this from the direct expansion solution

$$\sigma_1(y) \approx \sigma_1(0)\left[1 - \frac{y^2}{6x_0^2}(1 + 2x_0 z_0)\right];\ y \ll x_0, \tag{A8}$$

which follows from equation (A2) and expansion of equation (A6) (see eq. [32]).

An alternative, general approach is to use equation (A6) to derive an explicit differential equation for $\sigma(y)$ itself, in a manner analogous to the derivation of equation (30). The addition of curvature and acceleration effects makes the resulting expression quite complicated, and so we omit details here. In practice, however, for the models in Figure 11 and all computations here, both approaches are used, and found to be in good agreement, except near the x-axis, where either the direct approach or equation (A8) is used.

An analogous procedure for star 2 yields the variation of the associated surface density $\sigma_2(y)$ along the interaction front.

REFERENCES

Anders, E., & Grevesse, N. 1989, Geochim. Cosmochim. Acta, 53, 197
Arnaud, K. A. 1996, in ASP Conf. Ser. 101, Astronomical Data Analysis Software and Systems V, ed. G. Jacoby & J. Barnes (San Francisco: ASP), 17
Canto, J., Raga, A. C., & Wilkin, F. P. 1996, ApJ, 469, 729
Chevalier, R. A., & Imamura, J. N. 1982, ApJ, 261, 543
De Becker, M., Rauw, G., Pittard, J. M., Antokhin, I. I., Stevens, I. R., Gosset, E., & Owocki, S. P. 2004, A&A, 416, 221
Gayley, K. G., Owocki, S. P., & Cranmer, S. R. 1997, ApJ, 475, 786
Girard, T., & Willson, L.A. 1987, A&A, 183, 247
Giuliani, J. L., Jr. 1982, ApJ, 256, 624
Henley, D., Stevens, I., & Pittard, J. 2003, MNRAS, 346, 773
Huang, R. Q., & Weigert, A. 1982, A&A, 112, 281
Jansen, F., et al. 2001, A&A, 365, L1
Langer, S. H., Chanmugam, G., & Shaviv, G. 1981, ApJ, 245, L23
Luo, D., McCray, R., & MacLow, M. 1990, ApJ, 362, 267
Maeda, Y., Koyama, K., Yokogawa, J., & Skinner, S. 1999, ApJ, 510, 967
Mewe, R., Gronenschild, E. H. B. M., & van den Oord, G. H. J. 1985, A&AS, 62, 197
Mewe, R., Kaastra, J. S., & Liedahl, D. A. 1995, Legacy, 6, 16
Mewe, R., Lemen, J.R., & van den Oord, G. H. J. 1986, A&AS, 65, 511
Myasnikov, A. V., & Zhekov, S. A. 1993, MNRAS, 260, 221
Myasnikov, A.V., Zhekov, S. A., & Belov, N. A. 1998, MNRAS, 298, 1021
Pauldrach, A., Puls, J., & Kudritzki, R. 1986, A&A, 164, 86
Pittard, J. M. 1998, MNRAS, 300, 479
Pittard, J. M., & Corcoran, M. F. 2002, A&A, 383, 636
Pittard, J. M., & Stevens, I. R. 1997, MNRAS, 292, 298
———. 2002, A&A, 388, L20
Pittard, J. M., Stevens, I. R., Corcoran, M. F., Gayley, K. G., Marchenko, S.V., Rauw, G., & Torii, K. 2000, MNRAS, 319, 137
Pittard, J. M., Williams, P. M., Pollock, A. M. T., Skinner, S. L., Corcoran, M. F., & Moffat, A. F. J. 2002, A&A, 388, 335
Raassen, A. J. J., van der Hucht, K. A., Mewe, R., Antokhin, I. I., Rauw, G., Vreux, J.-M., Schmutz, W., & Güdel, M. 2003, A&A, 402, 653
Raymond, J. C., Cox, D. P., & Smith, B. W. 1976, ApJ, 204, 290
Stevens, I. R., Blondin, J. M., & Pollock, A. M. T. 1992, ApJ, 386, 265
Stevens, I. R., & Pollock, A. M. T. 1994, MNRAS, 269, 226
Usov, V. V. 1992, ApJ, 389, 635
van Hoof, P. A. M., Martin, P. G., & Ferland, G. J. 2000, in ASP Conf. Ser. 215, Cosmic Evolution and Galaxy Formation: Structure, Interactions, and Feedback, ed. J. Franco, L. Terlevich, O. Lopez-Cruz, & I. Aretxaga (San Francisco: ASP), 220
Vishniac, E. T. 1994, ApJ, 428, 186

Walder, R. 1995, in IAU Symp. 163, Wolf-Rayet Stars: Binaries, Colliding Winds, and Evolution, ed. K. A. van der Hucht & P. M. Williams (Dordrecht: Kluwer), 420
Walder, R., & Folini, D. 2000, Ap&SS, 274, 343
———. 2003, IAU Symp. 212, ed. K. van der Hucht, A. Herrero, & C. Esteban (San Francisco: ASP), 139
Waldron, W. L., Corcoran, M. F., Drake, S. A., & Smale, A.P. 1998, ApJS, 118, 217
Whitney, B. A, Wood, K., Bjorkman, J. E., & Wolff, M. J. 2003, ApJ, 591, 1049
Zhekov, S. A., & Skinner, S. L. 2000, ApJ, 538, 808